Numerical assessment of temperature effects on concrete failure behavior

Marianela Ripani, Sonia Vrech & Guillermo Etse

International Journal of Fracture

ISSN 0376-9429

Int J Fract
DOI 10.1007/s10704-018-0301-z

Springer

Int J Fract
https://doi.org/10.1007/s10704-018-0301-z

ORIGINAL PAPER

Numerical assessment of temperature effects on concrete failure behavior

Marianela Ripani · Sonia Vrech · Guillermo Etse

Received: 13 September 2017 / Accepted: 17 July 2018

Abstract This work focuses on the evaluation of temperature effects on concrete failure behavior and modes by means of a realistic thermodynamically consistent non-local poroplastic constitutive model, previously developed by the authors, which is modified in this work. In this regard, two original contributions are presented and discussed. Firstly, and based on significant published experimental results related to this very complex aspect such as the effects of temperature in concrete failure, a temperature dependent non-associated flow rule is introduced to the poroplastic constitutive model to more accurately account for the temperature dependent inelastic volumetric behavior of concrete in post-peak regime. This is crucial for improving overall model accuracy, particularly regarding the temperature effects on concrete released energy during degradation processes. Secondly, and more importantly, the explicit solution of the localization condition in terms of the critical hardening modulus is developed regarding the non-local poroplastic constitutive model reformulated in this work, which allows the analysis of localized failure modes in the form of discontinuous bifurcation of quasi-brittle porous materials like concrete under different temperature, hydraulic and stress state scenarios. Also numerical procedures are followed, which also allow the evaluation of temperature effects on the critical directions for localized failure or cracking which is performed in this work for a wide spectrum of stress states and temperatures. Both, undrained and drained hydraulic conditions are evaluated. The results in this work demonstrate the soundness of the proposed constitutive model modifications and of the derived explicit solution for the critical hardening modulus to accurately predict the temperature effects on both, concrete volumetric behavior, and on the failure modes and related critical cracking direction. They also demonstrate that concrete failure mode and critical localization directions are highly sensitive to temperature, particularly in the compressive regime.

Keywords Gradient poroplasticity · Discontinuous bifurcation · Failure · Concrete

M. Ripani · S. Vrech · G. Etse
CONICET, Argentinean Council for Scientific and Technical Researches, Buenos Aires, Argentina
e-mail: mripani@fi.uba.ar

M. Ripani
INTECIN, Faculty of Engineering, University of Buenos Aires, Buenos Aires, Argentina

S. Vrech (✉) · G. Etse
CEMNCI, University of Tucuman, San Miguel de Tucumán, Argentina
e-mail: svrech@hotmail.com

G. Etse
e-mail: getse@herera.unt.edu.ar

1 Introduction

Materials like soils and concrete have a quasi-brittle and very complex mechanical behavior when strong accumulations of inelastic strains take place. Under these critical conditions the evaluation and prediction

Published online: 26 July 2018

of the involved failure mode and, moreover, the transition point between brittle or localized and diffuse failure regimes becomes highly complex. This is a crucial aspect of material and structural failure mechanics due to severe consequences of brittle failure modes on the overall safety conditions of civil constructions.

On the other hand, when concrete is subjected to long term exposures of high temperatures, it takes place an irreversible degradation of two fundamental material properties, the elastic stiffness (thermal damage) and the material strength (thermal decohesion). Basically, the level of degradation depends on the maximum temperature reached. The experimental evidence, see Figs. 1 and 2, demonstrates the dramatic and substantial decrease of elastic modulus and Poisson's ratio as well as compressive and tensile strengths due to thermal actions. In addition, thermal degradation induces a much more severe microcracking in concrete. Consequently, and due to the tortuosity of the microcrack faces, the internal friction of concrete increases. This is particularly evident between 250 and 400 °C. As the temperature continues to rise, the microcracks converge in a macro fracture and the localized failure mode turns evident. Two other important effects of temperatures on concrete are the weight loss and the pore pressure variation. The weight loss is related to the porosity increase and is mainly attributed to humidity loss and spalling, see Janotka and Bagel (2002). Based on the experimental evidence by Kalifa et al. (2000), Mindeguia et al. (2010) and Pereira et al. (2011), it can be seen that the concrete pore pressure increases due to the temperature rise under fully undrained conditions up to a trigger temperature. Once this limit is reached, a severe micro cracking process developes in the surrounding skeleton which leads to a sudden and quick pore pressure loss. This cracking process and related pore pressure change is mainly responsible for the well-known concrete spalling that develops in the proximity to the surface subjected to the heating. From the available literature, it can be said that up to 200 °C only loss of evaporable water occurs while no significant change in concrete mechanical properties takes place (Mihashi et al. 1992). Between 200 and 500 °C the dehydration of calcium silicate hydrate (CSH) and calcium hydroxide ($Ca(OH)_2$) take place and therefore, the irreversible degradation of concrete mechanical properties is evidenced. It should be noted that in undrained states, the fluid mass content remains unchanged in the skeleton.

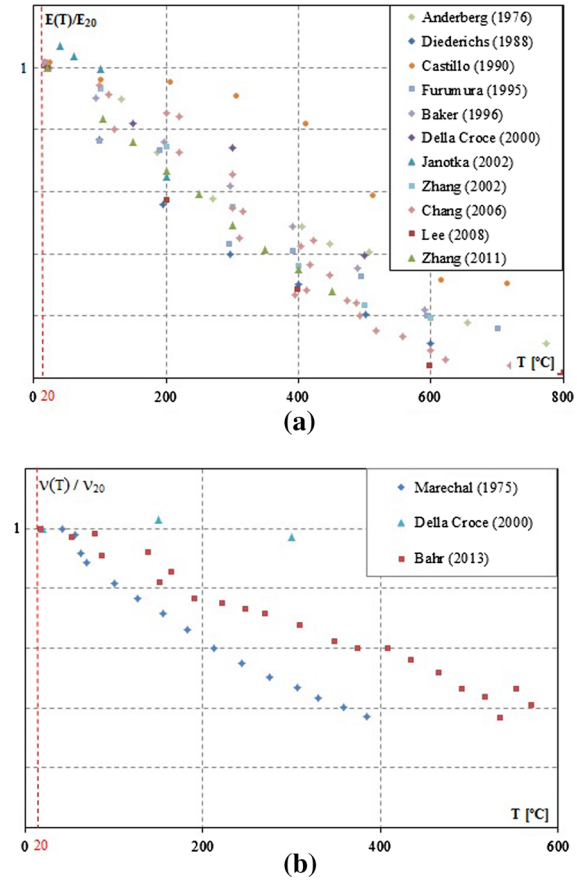

Fig. 1 Experimental data of **a** elastic modulus and **b** Poisson's ratio degradations with increasing temperature

Since the pioneer work by Rudnicki and Rice (1975) significant progress was made in understanding the performance of the discontinuous bifurcation condition in concrete materials under consideration of a wide spectrum of theoretical frameworks, see a.o. the works by Ortiz (1987), Ottosen and Runesson (1991), Ottosen et al. (1991), Kang and Willam (1999), Vrech and Etse (2006, 2012), Xotta et al. (2016), Jirásek and Rolshoven (2009a, b). All of them were related to room temperature conditions and also to non-porous -based material theories since under ambient temperature the influence of the pore pressure in mature concrete is nonsense.

In the framework of inelastic porous material theories, the discontinuous bifurcation condition was analyzed by means of different approaches and taking into account the influence of the Lode angle (Zhen et al. 2010), water content or fluid pressure (Runesson et al.

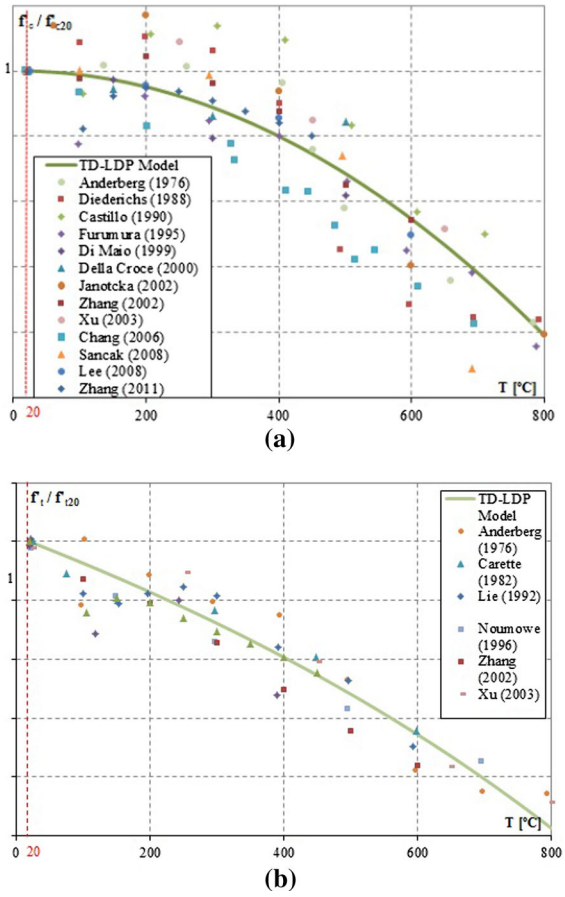

Fig. 2 Experimental data and TD-LDP numerical results of **a** compressive and **b** tensile strength degradation with increasing temperature

1996; Liu et al. 2005), porosity (Zhang et al. 2002), permeability (Zhang and Schrefler 2001), temperature (Sulem 2010), rheological effects (Henann and Kamrin 2014), etc. Actually, most of the published localization analyses in porous media are related to soils as the pore pressure and the saturation degree in this material play a very important role. Among others we may refer to the contributions by Sabatini and Finno (1996), Benallal and Comi (2002), Borja (2004), Ehlers et al. (2004), Kristensson and Ahadi (2005) and Schiava and Etse (2006), which are based on the consideration that discontinuous bifurcations may only occur in the solid phase. More recently, Mroginski and Etse (2014) performed a comprehensive analysis on the potentials for discontinuous bifurcation in partially saturated soils under consideration of arbitrary mechanical and hydraulic conditions.

Several proposals were made on constitutive theories for predicting failure behavior of concrete when subjected to thermomechanical actions. We may refer here to the contributions by Tenchev and Purnell (2005) which is based on a temperature dependent combination between the continuum damage and mixture theories, the one by Gawin et al. (2004) which considers a coupled thermo-chemical and mechanical damage formulation in the framework of the porous material theory to account for the hygro-thermo-chemomechanical behavior of high strength concrete (HSC) at elevated temperature, and the one by Gernay et al. (2013) which is based on the combination of elastoplasticity and damage theories and includes a generic transient creep mode. Most of the model contributions so far, related to both classical continua and porous media, are based on local formulations and, therefore, they suffer the well known shortcomings of the smeared-crack-based constitutive theories in softening regime, when the related differential equations turn ill-defined. In case of concrete subjected high temperature effects, the consideration of non-local, dissipative porous media-based constitutive theories is crucial to accurately account for both, the regularization of post-peak responses when concrete failure mode turns brittle, as well as the pore pressure effect in temperature dependent failure processes.

Recently, a non-local, gradient poroplastic material formulation for concrete under arbitrary termomechanical condition was proposed by Ripani et al. (2014). The so-called temperature-dependent Leon–Drucker–Prager model (TD-LDP model) considers two mechanisms in parallel to describe the thermomechanical degradation of concrete strength. On the one hand, a fracture energy-based mechanism accounting for the temperature-dependent strength to further develop active cracks in concrete. On the other hand, a gradient-based poroplastic mechanism which accounts for the thermomechanical strength of the concrete material/continua located between active cracks. This results in two characteristic lengths, one due to the gradient theory and the other one due to the fracture energy-released concept involved in the softening formulation. Both geometrical lengths are defined in terms of current temperature field and confining pressure. The predictive capabilities of the TD-LDP model in terms of strength and stiffness in pre-peak and peak regimes were demonstrated in Ripani et al. (2014) and is further demonstrated in Fig. 2, where the numerical prediction

of the variation of concrete maximum compressive and tensile strengths with temperature are compared with experimental results. However, this constitutive model, according to its current formulation is unable to accurately describe the relevant thermal dependency of concrete ductility in post-peak regime. This follows from the analysis of model predictions of recently pusblished experimental results on concrete failure behavior under different temperature conditions, see Hammoud et al. (2014) and Xargay et al. (2018).

This work involves two novel and original aspects. On the one hand, a modification of the constitutive equations of the TD-LDP model is proposed to more realistically reproduce the influence of both, temperature and confining pressure in the post-peak inelastic response of concrete in view of the recently published experimental results by Hammoud et al. (2014) and Xargay et al. (2018). To this end, the thermodynamically consistent volumetric non-associated flow rule is reformulated to account for the acting temperature and pressure. On the other hand, and very importantly, explicit solutions for localized failure modes are obtained in the framework of the Modified nonlocal gradient TD-LDP poroplastic model for concrete under consideration of arbitrary thermomechanical conditions and for both, undrained and drained states. These explicit solutions, expressed in terms of the critical hardening modulus for discontinuous bifurcation, allow determining the earliest hardening modulus for the onset of localized failure and cracking in concrete, and evaluating the temperature effects in the cracking initiation and orientation.

After a brief description of the theoretical framework of the considered gradient poroplastic theory for quasi-brittle materials in Sect. 2, the constitutive equations of the TD-LDP model and, particularly, the proposed modifications to more accurately capture the inelastic volumetric behavior in pre- and post-peak regimes of concrete and its temperature dependence are detailed in Sect. 3. Then, in Sect. 4 the attention focuses on the formulation of the discontinuous bifurcation condition in the form of localized failure, by means of numerical and analytical procedures. In parallel, the performance and properties of the localized failure indicator in concrete under different temperature and stress conditions are analyzed.

Both, the validation against experimental tests on temperature dependent failure behavior of concrete which is done in this work with the Modified TD-LDP model, and the assessments of the temperature effects on concrete localized failure modes obtained with this proposed model, demonstrate that concrete failure modes are strongly temperature-dependent. The temperature affects not only the potentials of localized failure, but also its critical directions, and the transition point between brittle and diffuse failure. The temperature sensitivity of localized failure modes in concrete is more significant in the compressive regime, while the potentials for discontinuous bifurcations are higher under plane strain conditions than under plane stress ones.

2 Thermodynamically consistent gradient poroplastic constitutive theory

In this section the thermodynamically consistent constitutive equations for gradient poroplastic materials under general non-isothermal conditions are summarized. Fundamental assumptions are:

- small strain kinematic,
- additive decompositions in elastic and plastic components of the rate forms of:

$$\dot{\boldsymbol{\varepsilon}} = \dot{\boldsymbol{\varepsilon}}^e + \dot{\boldsymbol{\varepsilon}}^p \quad \text{strain tensor,} \tag{1}$$

$$\dot{m} = \dot{m}^e + \dot{m}^p \quad \text{fluid mass content,} \tag{2}$$

$$\dot{s} = \dot{s}^e + \dot{s}^p \quad \text{entropy density,} \tag{3}$$

- inelastic behavior takes place in both, skeleton and porous phases,
- the scalar softening variable is the only one of nonlocal character.

The free energy density can be decomposed into three components, the elastic, the local plastic and the gradient plastic one

$$\psi\left(\boldsymbol{\varepsilon}^e, m^e, \theta, q_\alpha, \nabla q_\alpha\right) = \psi^e\left(\boldsymbol{\varepsilon}^e, m^e, \theta\right) + \psi^l\left(q_\alpha, \theta\right) + \psi^g\left(\nabla q_\alpha\right), \tag{4}$$

where θ is the relative temperature ($\theta = T - 20\ ^\circ\text{C}$, being T the acting temperature). The hardening/softening variables are represented by q_α, with the subscript $\alpha = p$ for the porous phase and $\alpha = s$ for the solid one. Non-local effects are computed as ∇q_α.

The constitutive equations for undrained and drained conditions, as well as the dissipative stresses can be derived from Eq. (4) regarding Coleman's relations, see

Ripani et al. (2014). Thus, the rate form of the constitutive relations in terms of total stresses, pore pressure and entropy density related to the solid skeleton under undrained conditions result

$$\dot{\boldsymbol{\sigma}} = \dot{\boldsymbol{\sigma}}' - M\frac{\dot{m}^e}{\rho_f}\boldsymbol{B} \quad \text{with} \quad \dot{\boldsymbol{\sigma}}' = \boldsymbol{E} : \dot{\boldsymbol{\varepsilon}}^e - \dot{\theta}\, \boldsymbol{E} : \boldsymbol{A}, \tag{5}$$

$$\dot{p} = \frac{M}{\rho_f}\dot{m}^e - M\boldsymbol{B} : \dot{\boldsymbol{\varepsilon}}^e + \rho_f \aleph \dot{\theta}, \tag{6}$$

$$\dot{s}_s = \boldsymbol{A} : \dot{\boldsymbol{\varepsilon}}^e - \aleph \dot{m}^e + \chi\, \dot{\theta} + \dot{s}_{fr}^{(q_\alpha)}, \tag{7}$$

being $\boldsymbol{E}$ the elastic tensor, M the Biot modulus, ρ_f the fluid phase density, $\boldsymbol{B} = b\boldsymbol{I}$ the Biot tensor with b the Biot coefficient and $\boldsymbol{I}$ the second order identity tensor, $\aleph$ the latent heat, χ the heat capacity while $\boldsymbol{A} = \alpha_\theta \boldsymbol{I}$ is the thermal expansion tensor, with α_θ the thermal expansion coefficient and $\dot{s}_{fr}^{(q_\alpha)}$ the rate of the unrecovered or "frozen" entropy, according Coussy (1995).

In drained hydraulic conditions, Eqs. (5) and (6) become

$$\dot{\boldsymbol{\sigma}} = \dot{\boldsymbol{\sigma}}' - \boldsymbol{B}\dot{p} \quad \text{with} \quad \dot{\boldsymbol{\sigma}}' = \boldsymbol{E}^s : \dot{\boldsymbol{\varepsilon}}^e - \dot{\theta}\, \boldsymbol{E}^s : \boldsymbol{A}^s, \tag{8}$$

$$\frac{\dot{m}^e}{\rho_f} = \boldsymbol{B} : \dot{\boldsymbol{\varepsilon}}^e + \frac{1}{M}\dot{p} - \frac{\rho_f}{M}\aleph\dot{\theta}, \tag{9}$$

where the elastic and thermal expansion tensors of the solid phase, $\boldsymbol{E}^s$ and $\boldsymbol{A}^s$ respectively, are defined as

$$\boldsymbol{E}^s = \boldsymbol{E} - M\,\boldsymbol{B} : \boldsymbol{B}, \quad \boldsymbol{A}^s = \rho_f \aleph \boldsymbol{B} - \boldsymbol{A}. \tag{10}$$

The constitutive equations for undrained and drained cases can be obtained from Eqs. (5) and (8), respectively, by replacing the rate of the plastic parameter from the consistency condition (see "Appendix A"). These constitutive equations result

$$\dot{\boldsymbol{\sigma}} = \boldsymbol{E}^{ep} : \dot{\boldsymbol{\varepsilon}} + {}^{m}\boldsymbol{E}^{ep}\,\dot{m} + \boldsymbol{E}^{g}\,\dot{\boldsymbol{\Phi}}^{g} + {}^{\theta}\boldsymbol{E}^{ep}\,\dot{\theta}, \tag{11}$$

$$\dot{\boldsymbol{\sigma}} = {}^{s}\boldsymbol{E}^{ep} : \dot{\boldsymbol{\varepsilon}} + {}^{md}\boldsymbol{E}^{ep}\,\dot{p} + {}^{d}\boldsymbol{E}^{g}\,\dot{\boldsymbol{\Phi}}_d^{g} + {}^{\theta d}\boldsymbol{E}^{ep}\,\dot{\theta}, \tag{12}$$

with the gradient yield functions $\dot{\boldsymbol{\Phi}}^g$ and $\dot{\boldsymbol{\Phi}}_d^g$ for the drained and undrained cases, respectively, and the material tensors $\boldsymbol{E}^{ep}$, ${}^{m}\boldsymbol{E}^{ep}$, $\boldsymbol{E}^{g}$, ${}^{\theta}\boldsymbol{E}^{ep}$, ${}^{s}\boldsymbol{E}^{ep}$, ${}^{md}\boldsymbol{E}^{ep}$, ${}^{d}\boldsymbol{E}^{g}$ and ${}^{\theta d}\boldsymbol{E}^{ep}$, as detailed in appendix A. In the particular case that the inelastic behavior is restricted to the solid phase, then ${}^{m}\boldsymbol{E}^{ep} = {}^{m}\boldsymbol{E}$, ${}^{md}\boldsymbol{E}^{ep} = {}^{md}\boldsymbol{E}$. Moreover, $\dot{m} = \dot{m}_e$.

3 The modified TD-LDP model for temperature-dependent concrete failure behavior

In this section, the constitutive equations of the Leon–Drucker–Prager model (TD-LDP model) proposed by Ripani et al. (2014) for open gradient poroplastic materials like mature concrete under non-isothermal conditions are modified to more accurately and realistically predict the temperature dependent volumetric dilatation of concrete under arbitrary thermomechanical conditions. Firstly, the fundamental equations of the TD-LDP model is refreshed. Then, the proposed temperature and pressure dependent non-associated flow rule is described.

3.1 Failure criterion and yield condition in pre- and post-regimes

Failure criterion and yield surfaces of the TD-LDP model are summarized by following equations, respectively

$$\Gamma\left({}^{*}\sigma', {}^{*}\tau, \theta\right) = \frac{3}{2}\alpha(\theta)\,{}^{*}\tau^2 + \beta(\theta) n_0 \left(\frac{{}^{*}\tau}{\sqrt{6}} + {}^{*}\sigma'\right) - c_0 = 0\,, \tag{13}$$

$$\Phi\left({}^{*}\sigma', {}^{*}\tau, \theta, {}^{h}Q, {}^{s}Q\right) = \frac{3}{2}\,\alpha(\theta)\,{}^{*}\tau^2 + \beta(\theta)\, n_0\, {}^{h}Q \left(\frac{{}^{*}\tau}{\sqrt{6}} + {}^{*}\sigma'\right) - {}^{h}Q\,{}^{s}Q = 0, \tag{14}$$

with the normalized Haigh Westergaard effective volumetric and deviatoric stress coordinates ${}^{*}\sigma' = \frac{I_1}{3f_c'} + b\frac{p}{f_c'}$ and ${}^{*}\tau = \frac{\sqrt{2J_2}}{f_c'}$ respectively, being I_1 the first invariant of total stress tensor, J_2 the second invariant of deviatoric stress tensor and f_c' the uniaxial compressive strength. Parameters n_0 and c_0, corresponding to the friction and cohesion of concrete at room temperature, are defined as $n_0 = \frac{3}{2}\frac{\left(f_c'^2 - f_t'^2\right)}{f_c' f_t'}$ and $c_0 = 1$ respectively, with f_t' the uniaxial tensile strength. Moreover, $\alpha(\theta)$ and $\beta(\theta)$ are the so-called temperature-dependent functions. Their expressions as well as those corresponding to the evolution of the hardening and softening dissipative stresses, ${}^{h}Q$ and ${}^{s}Q$ respectively, are detailed in Ripani et al. (2014).

The degradation induced by temperature strongly affects the material stiffness, as demonstrated by exper-

imental evidence in Fig. 1. According to Ripani et al. (2014), the dependency of the concrete elasticity modulus E and the Poisson's ratio ν on the temperature level are approximated by the following linear functions, respectively,

$$E = E_0 \left(1 - \alpha_E \, \theta\right), \tag{15}$$

$$\nu = \nu_0 \left(1 - \alpha_\nu \, \theta\right), \tag{16}$$

being E_0 and ν_0 the elasticity modulus and Poisson's ratio at 20 °C, while α_E and α_ν represent the corresponding degradation parameters.

3.2 Temperature and pressure dependent plastic potential

To accurately reproduce the strongly temperature and confining pressure dependent inelastic volumetric behavior of concrete, the following expression is proposed in this work for the plastic potential of the Modified TP-LDP model

$$\Phi^* \left({}^*\sigma', {}^*\tau, \theta, {}^h Q, {}^s Q\right) = \Phi + \beta(\theta) \, n_0 \left[(\eta - 1) \, {}^*\sigma'\right] = 0 \,, \tag{17}$$

with η the volumetric non-associativity degree, which varies according to the acting effective volumetric stress and temperature level according to

$$\eta({}^*\sigma', \theta) = \frac{1}{2} - \frac{1}{4}\left[\cos\left(\pi \frac{{}^*\sigma'_{min} + {}^*\sigma'}{{}^*\sigma'_{max} - {}^*\sigma'_{min}}\right) + \cos\left(\pi \frac{\theta_{min} + \theta}{\theta_{max} - \theta_{min}}\right)\right] \tag{18}$$

when $-1.5 \geq {}^*\sigma' \geq 0$ and $0 \leq \theta \leq 480$ °C, as can be seen in Fig. 3. Outside these limits the function takes constant values, corresponding to the maximum and minimum ${}^*\sigma'$ and θ.

Figure 4 shows the Finite Element predictions obtained with the Modified TD-LDP model of post-peak lateral deformations of concrete specimens subjected to residual uniaxial compression tests after being subjected to different temperatures. The numerical results in terms of lateral deformations (ϵ_r) agree very well with the experimental data by Hammoud et al. (2014) and Xargay et al. (2018), solving the deficiencies of the previous model as can be observed in Fig. 4a. In the computational analyses performed in this work, the dual mixed constant strain triangular (CST) FE formulation for thermodynamically consistent gradient

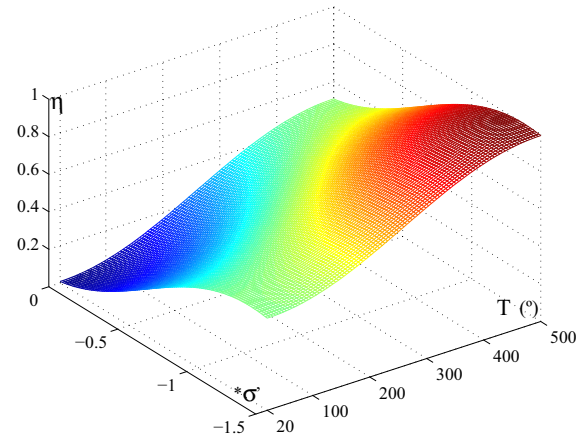

Fig. 3 Variation of the non-associativity degree in terms of effective volumetric stress and temperature level

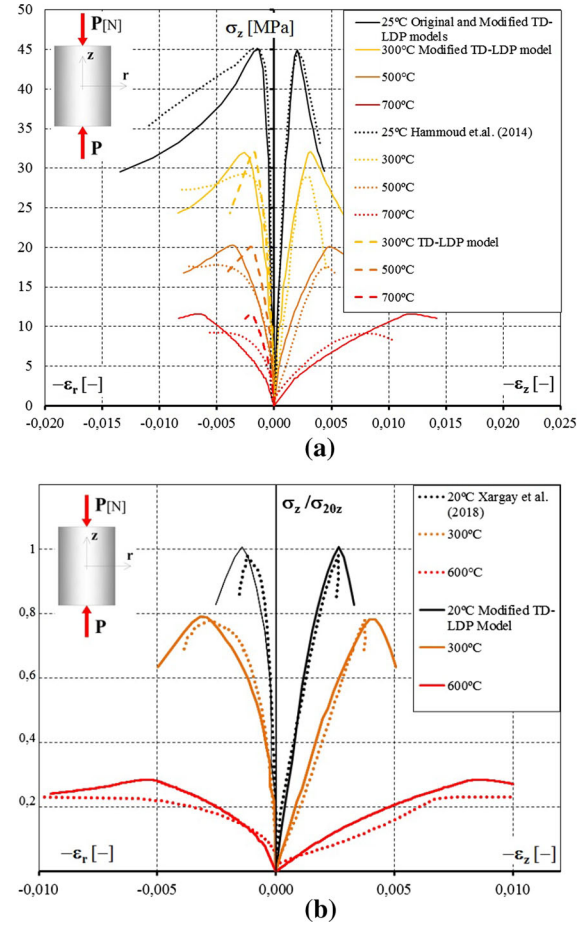

Fig. 4 Numerical predictions of uniaxial compression tests under increasing temperatures: **a** former and Modified TD-LDP models, and experimental results by Hammoud et al. (2014) and **b** modified TD-LDP model and experimental results by Xargay et al. (2018)

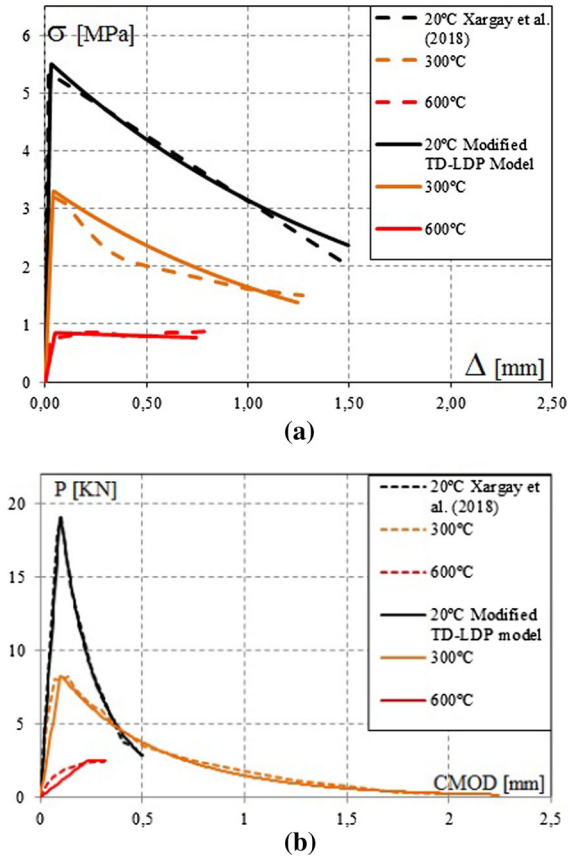

Fig. 5 Numerical predictions of experimental results by Xargay et al. (2018) **a** splitting tensile test and **b** three point bending test

plasticity proposed by Vrech and Etse (2007, 2009) is used.

As can be observed in Fig. 5a, b, very good agreement has also been achieved for the experimental results performed by Xargay et al. (2018) of temperature-dependent splitting tensile tests and three point bending tests, respectively. The results in these figures are depicted in terms of the stress versus crack opening displacements, in case of the splitting tensile tests, and of load versus crack mouth opening displacement (CMOD), in case of the three point bending tests. As can be observed in these figures, the Modified TD-LDP model leads to accurate predictions of the stiffness, and of the peak and residual stresses/loads in all different tests and temperatures.

Figure 6 illustrates the Modified TD-LDP model predictions of the temperature dependency of the fracture energy released during post-peak regimes of uniaxial tensile tests under residual conditions. It can be

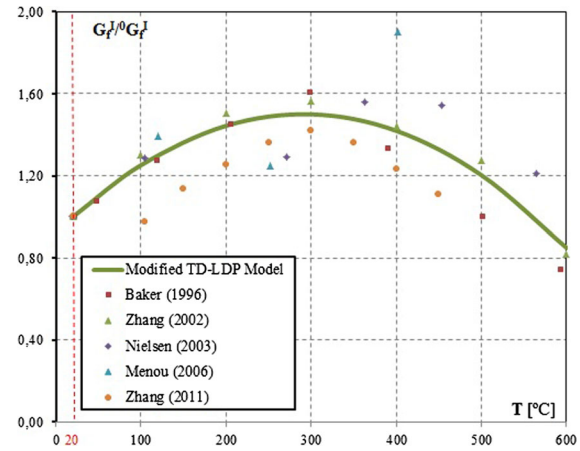

Fig. 6 Fracture energy released under Mode I type of failure. Experimental data versus predictions of the Modified TD-LDP model

observed that the numerical results, based on the proposed temperature and pressure dependent volumetric non-associativity degree reproduce very accurately the experimentally observed form of the thermal dependency denoted by the fracture energy released. In general, it can be observed an increment of the released fracture energy under mode I with temperature up to 400 °C, approximately, follows by a strong reduction with further temperature increments. The results in Figs. 4 and 6 demonstrate the soundness of the proposed Modified TD-LDP model, particularly regarding its degree of volumetric non-associativity, and the resulting temperature dependent inelastic volumetric behavior of concrete.

4 Temperature-dependent localized failure condition in gradient-based poroplastic materials

In this section the discontinuous bifurcation analysis for poroplastic materials is carried out regarding undrained and drained conditions.

From the Hadamard's compatibility conditions Hadamard (1903) and the conservation law ($\dot{m} + \nabla \cdot \boldsymbol{w} = 0$), the jumps of the kinematic variables of a porous medium can be written as

$$[\![\dot{\boldsymbol{\varepsilon}}]\!] = [\![\nabla \dot{\boldsymbol{u}}]\!] = \frac{1}{2}[\![\nabla \dot{\boldsymbol{u}} + (\nabla \dot{\boldsymbol{u}})^T]\!] = \frac{1}{2}[\![\boldsymbol{g}_s \otimes \boldsymbol{n} + \boldsymbol{n} \otimes \boldsymbol{g}_s]\!], \tag{19}$$

$$[\![\nabla \cdot \boldsymbol{w}]\!] = -[\![\dot{m}]\!] = \boldsymbol{g}_p \cdot \boldsymbol{n}, \tag{20}$$

being $\dot{\boldsymbol{u}}$ the velocity vector, $\boldsymbol{g}_s$ and $\boldsymbol{g}_p$ the skeleton and porous polarization vectors respectively, $\boldsymbol{w}$ the relative flow vector and $\boldsymbol{n}$ the normal to the discontinuity surface S. In quasi-static problems, the jumps of the hydraulic field (represented through the pore pressure p), the total stress $\boldsymbol{\sigma}$ and the temperature θ are obtained applying Hadamard relation and take the form

$$c\,[\![\nabla p]\!] + [\![\dot{p}]\!]\boldsymbol{n} = \boldsymbol{0}, \tag{21}$$

$$[\![\dot{\boldsymbol{\sigma}}]\!] \cdot \boldsymbol{n} = \boldsymbol{0}, \tag{22}$$

$$c[\![\nabla\theta]\!] + [\![\dot{\theta}]\!]\boldsymbol{n} = \boldsymbol{0}. \tag{23}$$

Taking into account the local entropy balance (see, Ripani et al. 2014)

$$\theta\left[\rho\dot{s} + \nabla \cdot \left(s_f\,\boldsymbol{w}\right)\right] = \rho r - \nabla \cdot \boldsymbol{h} + \varphi^M \tag{24}$$

where s_f is the fluid mass entropy density, r the volume heat sources, $\boldsymbol{h}$ the heat flux vector and φ^M the mechanical dissipation, it can be demonstrated that the simultaneous fulfillment of Eqs. (23) and (24) requires the continuity of the temperature time rate across any eventual discontinuity surface, see Coussy (1995).

Under undrained boundary conditions, the variation of the fluid mass content is null in the solid skeleton, thus $\dot{m} = 0$, and the pore pressure can be obtained from the kinematics of the solid phase.

In the following, the localized failure condition is analyzed departing from the jump of the total stress tensor across the discontinuity surface. Thereby, the total stress tensor should satisfy the equilibrium condition $\nabla \cdot \dot{\boldsymbol{\sigma}} = 0$. Instability conditions are evaluated through the condition for the loss of ellipticity of the differential equations of equilibrium. Following Svedberg and Runesson (1997), Tsagrakis et al. (2003)and Abellan and de Borst (2006), this condition is analyzed through wave propagation analysis from which the solutions of the field variables i.e. displacements, fluid mass content, plastic multiplier and temperature, are obtained as

$$\begin{pmatrix} \dot{\boldsymbol{u}} \\ \dot{m} \\ \dot{\lambda} \\ \dot{\theta} \end{pmatrix} = \begin{pmatrix} \dot{\boldsymbol{U}}(t) \\ \dot{M}(t) \\ \dot{L}(t) \\ \dot{\Theta}(t) \end{pmatrix} \exp\left(\frac{i2\pi}{\delta}\boldsymbol{n} \cdot \boldsymbol{x}\right) \tag{25}$$

being $\boldsymbol{x}$ the position vector (in Cartesian coordinates) and δ the wave length. The wave solutions are represented by $\dot{\boldsymbol{U}}(t), \dot{M}(t), \dot{L}(t)$ and $\dot{\Theta}(t)$. From Eq. (25) and considering gradient isotropy, the non-local component of the plastic consistency in Eq. (39) (see "Appendix A"), can be expressed as

$$\dot{\Phi}^g = -\underbrace{l_c^2\,\Phi_{,Q_\alpha}\Phi^*_{,Q_\alpha}H^g\left(\frac{2\pi}{\delta}\right)^2}_{h^g}\underbrace{\dot{L}(t)\,\exp\left(\frac{i2\pi}{\delta}\boldsymbol{n}\cdot\boldsymbol{x}\right)}_{\dot{\lambda}} \tag{26}$$

where h^g is called generalized gradient modulus and the symbology $a_{,b}$ indicates partial derivative of a respect to b. Then, the equilibrium condition across the discontinuity surface enforces $(2\pi/\delta)^2\,\boldsymbol{Q}^{ep}_{nl}\cdot\dot{\boldsymbol{U}}(t) = \boldsymbol{0}$, being $\boldsymbol{Q}^{ep}_{nl}$ the non-local acoustic tensor, which in the undrained case is

$$\begin{aligned}\boldsymbol{Q}^{ep}_{nl} = \boldsymbol{n}\cdot\Bigg\{\boldsymbol{E} - \frac{1}{(h+h^g)}\Bigg[&\boldsymbol{E}:\Phi^*_{,\boldsymbol{\sigma}}\otimes\Phi_{,\boldsymbol{\sigma}}:\boldsymbol{E} \\ &-\left(\frac{M}{\rho_f}\right)^2\Phi_{,p}\,\Phi^*_{,p}\,\boldsymbol{B}\otimes\boldsymbol{B} \\ &+\frac{M}{\rho_f}(\Phi_{,p}\,\boldsymbol{E}:\Phi^*_{,\boldsymbol{\sigma}}\otimes\boldsymbol{B} \\ &+\Phi^*_{,p}\,\boldsymbol{B}\otimes\Phi_{,\boldsymbol{\sigma}}:\boldsymbol{E})\Bigg]\Bigg\}\cdot\boldsymbol{n}\end{aligned} \tag{27}$$

and the localized failure indicator results

$$\det\left(\boldsymbol{Q}^{ep}_{nl}\right) = 0. \tag{28}$$

4.1 Special case: drained condition

In this case, porous media are subjected to pore pressure gradients. Thus, the relative flow vector $\boldsymbol{w}$ should remain continuous, i.e. $[\![\boldsymbol{w}]\!] = 0$. Then, from Darcy's law follows that $[\![\nabla p]\!] = 0$ and consequently, from Eq. (21) results $[\![\dot{p}]\!] = 0$. Consequently, from Eq. (43) follows

$${}^d\boldsymbol{Q}^{ep}_{nl} = \boldsymbol{n}\cdot\left[\boldsymbol{E}^s - \frac{1}{(h_d+h^g)}\left(\Phi_{,\boldsymbol{\sigma}}:\boldsymbol{E}^s\otimes\boldsymbol{E}^s:\Phi^*_{,\boldsymbol{\sigma}}\right)\right]\cdot\boldsymbol{n}. \tag{29}$$

In case of the Modified TD-LDP model, the derivatives in Eqs. (27) and (29), for undrained and drained case, respectively, result

$$\Phi_{,\boldsymbol{\sigma}} = \left[3\alpha(\theta) + \frac{\beta(\theta)\, n_0}{\sqrt{6}\,{}^*\tau}\right]\frac{1}{f_c'^2}\boldsymbol{S} + \frac{\beta(\theta)\, n_0}{3 f_c'}\boldsymbol{I} \quad (30)$$

$$\Phi^*{}_{,\boldsymbol{\sigma}} = \left[3\alpha(\theta) + \frac{\beta(\theta)\, n_0}{\sqrt{6}\,{}^*\tau}\right]\frac{1}{f_c'^2}\boldsymbol{S} + \frac{\beta(\theta)\, \eta\, n_0}{3 f_c'}\boldsymbol{I}, \quad (31)$$

$$\Phi_{,p} = -\frac{\beta(\theta)\, n_0}{f_c'}; \quad \Phi^*{}_{,p} = -\frac{\beta(\theta)\, \eta\, n_0}{f_c'}, \quad (32)$$

being $\boldsymbol{S}$ the deviatoric stress tensor.

5 Localized failure analysis in concrete subjected to temperature with the modified TD-LDP model

In this section, different procedures are followed to evaluate the performance of the condition for discontinuous bifurcation in the form of localized failure in concrete under different temperature conditions. For this purpose, the constitutive equations of the Modified TD-LDP model are considered.

5.1 Numerical procedure

The numerical analysis of localized failure conditions in concrete subjected to high temperature in the framework of the Modified TP-LDP model follows from Eqs. (27) or (29), for drained or undrained case, respectively.

In this analysis, the concrete material properties indicated in Table 1 are assumed, while the internal parameters of the Modified TD-LDP constitutive

Table 1 Material properties and internal parameters adopted for the numerical analysis

Elastic modulus—E	19305.3 MPa
Poisson's ratio—ν	0.2
Compressive strength—f_c'	22.0 MPa
Tensile strength—f_t'	2.7 MPa
Temperature-dependent functions—γ_1; γ_2	0.00126; 0.00056 °C^{-1}
Degradation parameters—α_E; α_ν	0.0014; 0.001 °C^{-1}

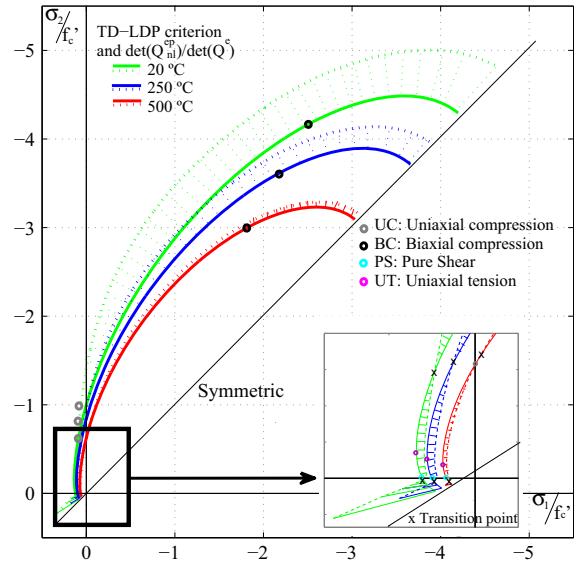

Fig. 7 Normalized localization indicators in normal direction to the modified TD-LDP maximum strength criterion for variable temperature under plane stresses

model coincide with those presented in Ripani et al. (2014).

In Figs. 7 and 8 the variation of the Normalized Localization Indicator (NLI) $\det\left(\boldsymbol{Q}_{nl}^{ep}\right)/\det\left(\boldsymbol{Q}^{e}\right)$, along the maximal strength criterion under plane stress and plain strain conditions, is evaluated for three different temperatures: T = 20, 250 and 500 °C. Note that at temperatures of 20 and 250 °C the system is assumed undrained, while at 500 °C, drained hydraulic conditions are assumed. These assumptions are based on the experimental results by Kalifa et al. (2000), Mindeguia et al. (2010), Hager (2013) and Zhang and Davie (2013) that have clearly demonstrated that the pore pressure in mature concrete subjected to heating increases continuously up to a threshold temperature of about 250 °C. Beyond this temperature, concrete pore pressure strongly decreases to practically zero. This experimental evidence supports the conclusion that due to the severe damage in the mortar matrix caused by the heating beyond the threshold temperature 250 °C, drained hydraulic conditions arise in the porous medium representing the concrete.

For each stress state on the maximum strength surface of the Modified TD-LPD model, the scaled values of NLI are represented in the normal direction to this surface, see Figs. 7 and 8. In case NLI > 0 for any arbitrary stress state on the maximum strength crite-

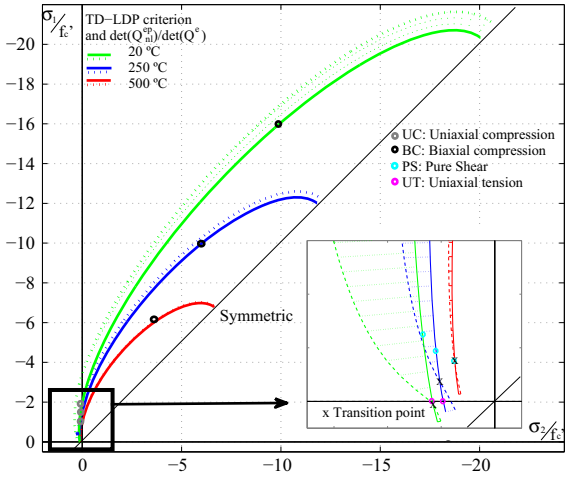

Fig. 8 Normalized localization indicators in normal direction to the modified TD-LDP maximum strength criterion for variable temperature under plane strains

rion of the Modified TD-LDP model, this means that instead of localized failure mode, a diffuse failure mode takes place in this particular stress state on the maximum strength surface. If NLI $= 0$, means that this critical stress state on the maximum strength surface does not only signalizes the peak strength of concrete, but also that a localized failure mode is occurring. If NLI < 0, means that the localized failure mode has occurred before reaching the maximum strength of concrete during the considered loading history, i.e. during the hardening or pre-peak regime.

Main conclusions arising from the results in Figs. 7 and 8 are:

- The potentials of localized failure as defined by NLI (length of the normal vectors to the strength surfaces) strongly increase with increasing temperature.
- The highest potential of localized failure is observed under plane strains and T $= 500\,^{\circ}$C, for all stress states on the maximum strength surface.
- As the temperature increases, the extension of the portion of the maximum strength surface associated to localized failure modes, enlarges.
- The zone of the maximum strength surface associated to localized failure appears in the compression-tension regime. The case of plane stress under 500 °C is the most critical case for discontinuous bifurcation as the portion of the maximum strength surface associated to this failure mode enters in the compression-compression regime.

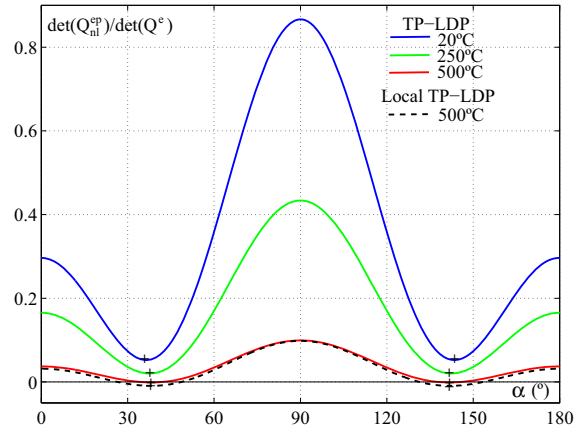

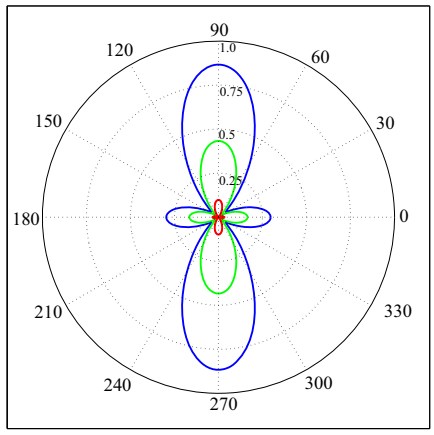

Fig. 9 Localization analysis with the Modified TD-LDP model at the peak of the uniaxial compression test for different temperatures, under plane stress state

Figures 9, 10 and 11 show the performance of the NLI at peak of the uniaxial compression, biaxial compression and uniaxial tensile tests, respectively, under plane stresses. From Figs. 9 and 10 follow that the most critical directions for localization varies with temperature while the potentials for localization increases with temperature. Moreover, in the uniaxial compression test (Fig. 9), the localization condition is fulfilled for 500 °C. In this figure can also be observed that the local version of the Modified TD-LDP model, i.e. without the gradient terms, leads to very similar predictions as the non-local Modified TD-LDP model in terms of the NLI performance. This is because, the gradient characteristic length of the Modified TD-LDP model approaches zero in this stress case which is associated to small confining pressure. In the biaxial compression

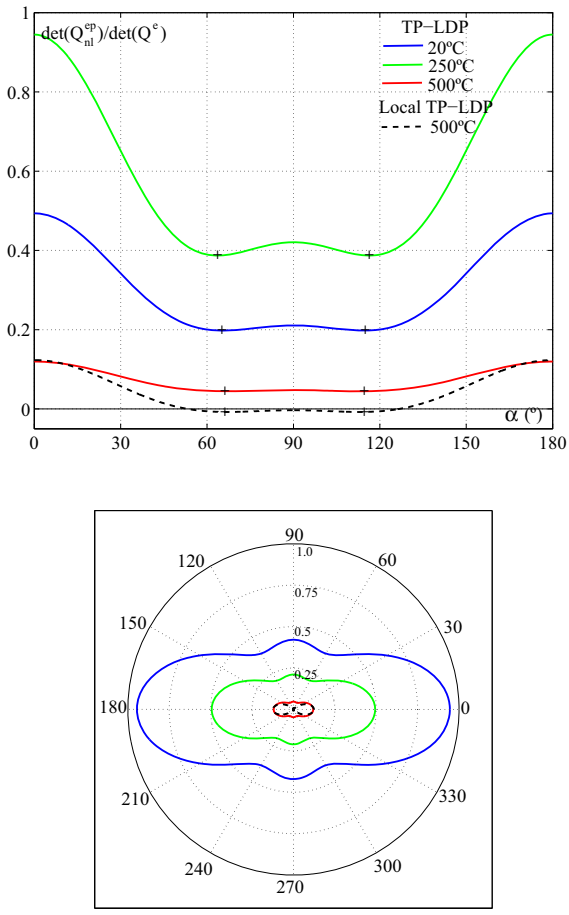

Fig. 10 Localization analysis with the modified TD-LDP model at the peak of the biaxial compression test for different temperatures, under plane stress state

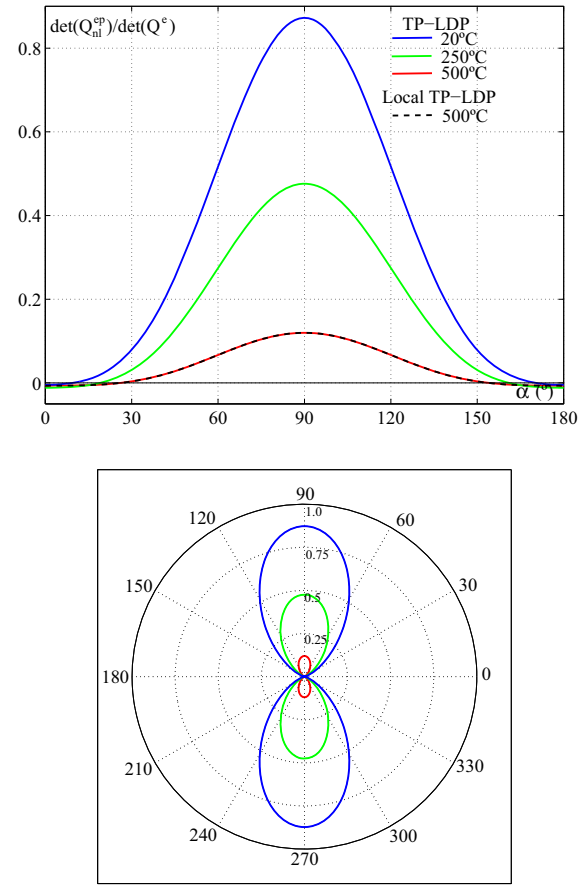

Fig. 11 Localization analysis with the Modified TD-LDP model at the peak of the uniaxial tensile test for different temperatures, under plane stress state

case (Fig. 10), the difference between the local and non-local Modified TD-LDP model predictions of the NLI for 500 °C is relevant as the confining pressure (and the gradient characteristic length) is large. Although both model versions lead to the same critical directions for localization, the discontinuous bifurcation condition is not fulfilled in the fracture energy- and gradient-based poro-plastic model considered in this work. Figure 12 shows the NLI performance at peak of the uniaxial compression test under plane strains. When comparing these results with those in Fig. 9 it can be concluded that the out of plane stress which develops in the plane strain case plays an important role in stabilizing the failure mode at peak of the uniaxial compression test as no localization takes place, including the case of 500 °C. Nevertheless, from Figs. 9, 10, 11 and 12 it can be concluded that temperature strongly damages and destabilizes concrete performance, leading to high localized failure potentials. Full 3D variations of the NLI performances at peak stresses of the four tests considered in these numerical analyses and under both, plane strains and plain stresses, are shown in Figs. 13, 14, 15 and 16, while the resulting critical localization directions are shown in Table 2, whereby the cases related to localized failure are underlined. Following conclusions are obtained from Figs. 9, 10, 11, 12, 13, 14, 15, 16 and Table 2:

– The results confirm that at 500 °C strong degradation of the NLI positiveness takes place for all possible wave propagation directions, indicating strong increase of concrete localization potentials.
– The degradation of overall concrete mechanical features under increasing temperature (area below

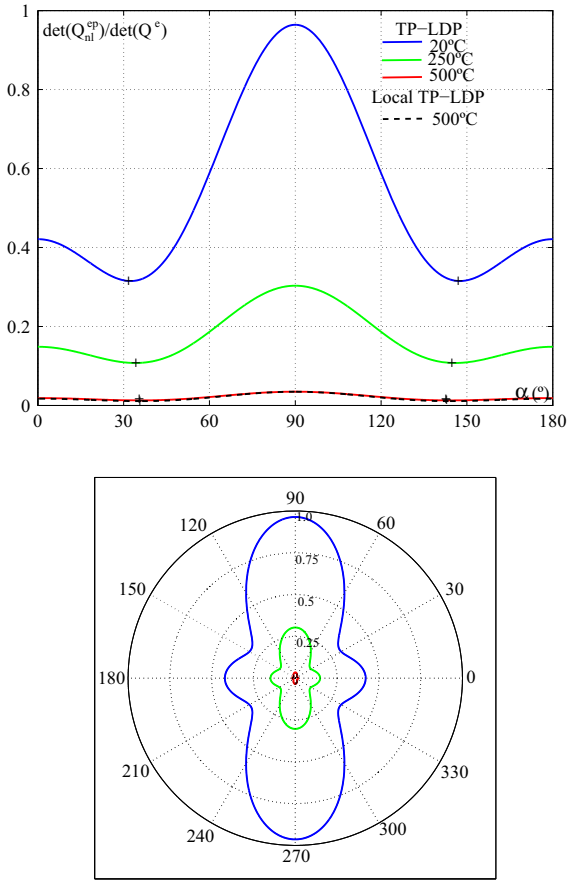

Fig. 12 Localization analysis with the Modified TD-LDP model at the peak of the uniaxial compression test for different temperatures, under plane strain state

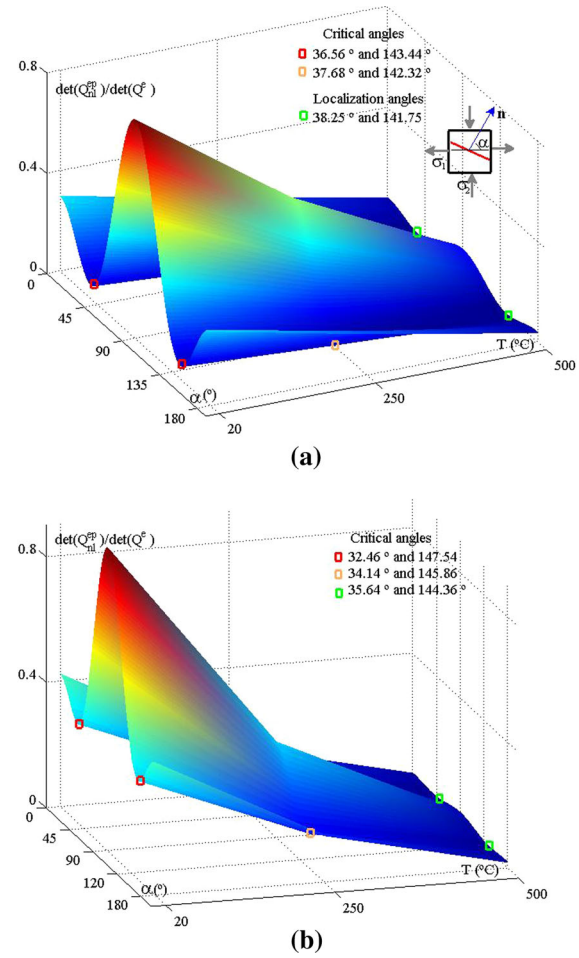

Fig. 13 Performance of the normalized localization indicator at peak stress of the uniaxial compression test for variable temperatures. **a** Plane stress state, **b** plane strain state

the NLI vs. α curves) is more severe in plane strains than plan stresses. The reason for this is the full 3D stress state that develops under plain strains which leads to a volumetric stiffness degradation due to temperature.

– Localized failure forms appear mostly under plane stresses in both, pure shear test (for all different temperatures), and uniaxial compression test (for 500 °C). Under plane strains, localized failure takes place only in the pure shear test and for 500 °C.

5.2 Analytical procedure

Explicit solutions for the critical hardening modulus in localization and the corresponding critical directions were developed by Ottosen and Runesson (1991) and Ottosen et al. (1991), by means of Lagrange multipliers. These solutions were applied to quasi-brittle materials and gradient continua by Vrech and Etse (2012) and also to temperature-independent gradient porous media by Mroginski and Etse (2014).

In this work, the analytical solutions for discontinuous bifurcation are derived for temperature dependent gradient poroplastic materials like concrete. Only the undrained case will be developed as the analytical solutions for the drained case can be deducted from the undrained one when $M = 0$.

The solution of the smallest eigenvalue of $\boldsymbol{Q}_{nl}^{ep}$ in Eq. (27) with respect to the metric defined by the inverse to the elastic acoustic tensor $[\boldsymbol{Q}^e]^{-1}$ (being $\boldsymbol{Q}^e = \boldsymbol{n} \cdot \boldsymbol{E} \cdot \boldsymbol{n}$) leads to the following localization condition

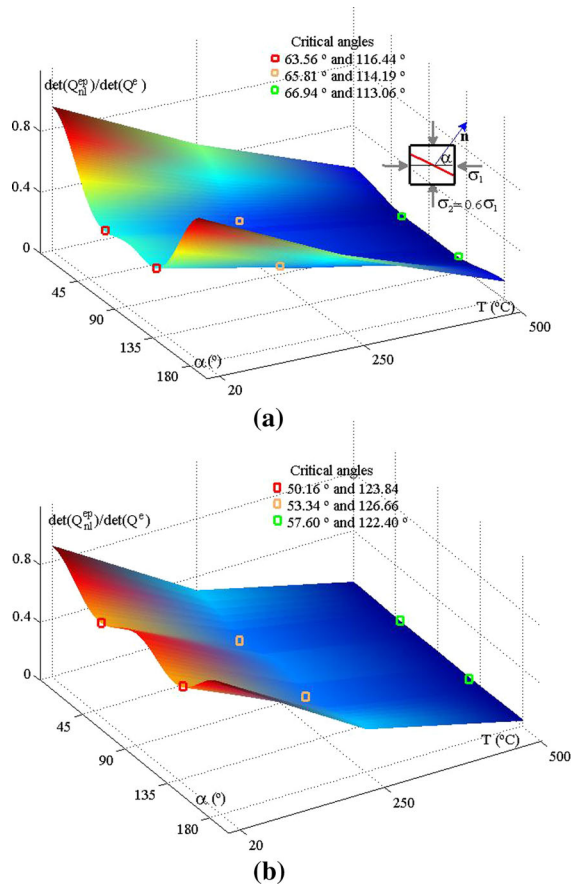

Fig. 14 Performance of the normalized localization indicator at peak stress of the biaxial compression test for variable temperatures. **a** Plane stress state, **b** plane strain state

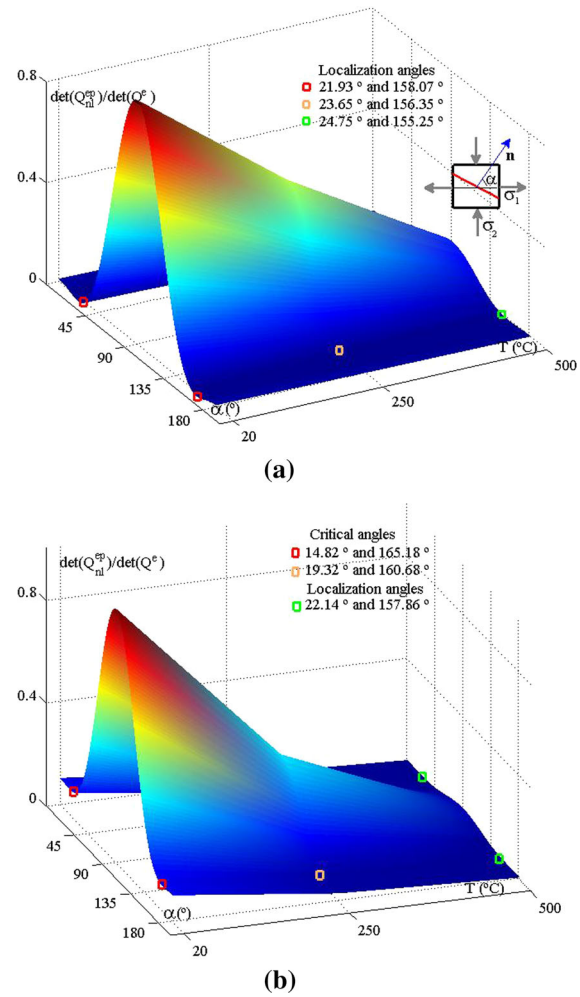

Fig. 15 Performance of the normalized localization indicator at peak stress of the pure shear test for variable temperatures. **a** Plane stress state, **b** plane strain state

$$\overline{H}^{l} - \left(\boldsymbol{Q}^{e}\right)^{-1} \boldsymbol{a} \otimes \boldsymbol{b} + \left(\frac{M}{\rho_f}\right)^{2} \left(\boldsymbol{Q}^{e}\right)^{-1} \boldsymbol{c} \otimes \boldsymbol{d} - \frac{M}{\rho_f} \left(\boldsymbol{Q}^{e}\right)^{-1} (\boldsymbol{c} \otimes \boldsymbol{a} + \boldsymbol{d} \otimes \boldsymbol{b}) - \frac{M}{\rho_f} \left(\Phi_{,\boldsymbol{\sigma}} : \boldsymbol{B}\, \Phi^{*}_{,p} - \rho_f \Phi_{,p} \boldsymbol{B} : \Phi^{*}_{,\boldsymbol{\sigma}} + \Phi_{,p} \Phi^{*}_{,p}\right) + \Phi_{,\boldsymbol{\sigma}} : \boldsymbol{E} : \Phi^{*}_{,\boldsymbol{\sigma}} + h^{g} = 0 \tag{33}$$

with

$$\boldsymbol{a} = \boldsymbol{n} \cdot \boldsymbol{E} : \Phi^{*}_{,\boldsymbol{\sigma}}, \qquad \boldsymbol{b} = \Phi_{,\boldsymbol{\sigma}} : \boldsymbol{E} \cdot \boldsymbol{n}, \tag{34}$$

$$\boldsymbol{c} = \Phi_{,p}\, \boldsymbol{n} \cdot \boldsymbol{B}, \qquad \boldsymbol{d} = \Phi^{*}_{,p} \boldsymbol{B} \cdot \boldsymbol{n}. \tag{35}$$

The critical hardening modulus and their associated localization directions are defined as $\overline{H}^{l}_{crit} = max\left[\overline{H}^{l}(\boldsymbol{n})\right]$.

Explicit solutions are evaluated by means of the Lagrange's multiplier method proposed by Ottosen and Runesson (1991), which evaluates the extreme propertiesof

$$L = \frac{\overline{H}^{l}_{crit}}{4G} + \wp \left(\boldsymbol{n}_1{}^2 + \boldsymbol{n}_2{}^2 + \boldsymbol{n}_3{}^2 - \boldsymbol{1}\right), \tag{36}$$

where $\wp$ is the Lagrange multiplier and G the shear modulus. In appendix B, critical hardening modulus and the corresponding localization directions are evaluated for all stress states on the maximum strength surface of the Modified TD-LDP model. It is important to highlight that critical hardening modulus as well as the corresponding critical directions not only depends on

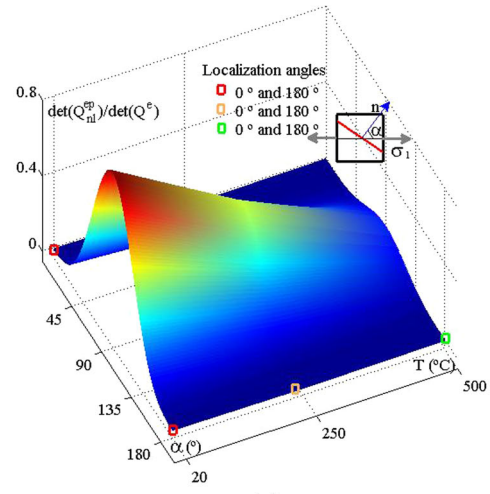

(a)

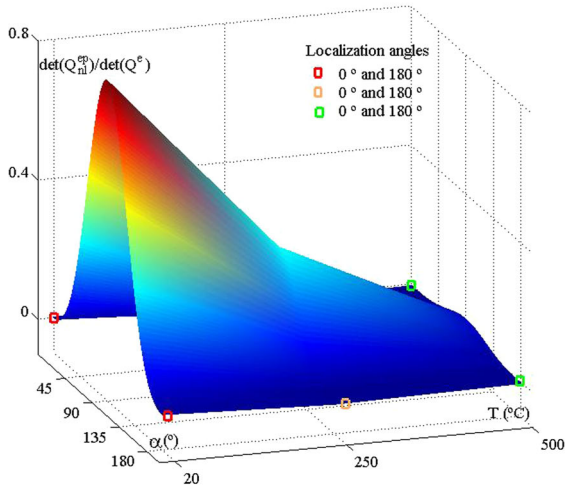

(b)

Fig. 16 Performance of the normalized localization indicator at peak stress of the uniaxial tensile test for variable temperatures. **a** Plane stress state, **b** plane strain state

the porous medium features but also on the temperature, because the elastic parameters and the derivatives of the loading function and plastic potential involved in their calculations strongly depend on these variables.

6 Conclusions

In this work, a reformulation of the non-local thermodynamically consistent TD-LDP model for concrete subjected to arbitrary mechanical and thermal loading was presented with the purpose to improve its accuracy for predicting the temperature effects in the volumetric dilatancy and lateral deformation of concrete during the post-peak regime. Comparisons presented with recently published experimental results confirm the soundness of the proposed Modified TD-LDP model for predicting the temperature-dependent failure behavior of concrete in the compressive and tensile regimes.

On the other hand, explicit solutions for the critical hardening modulus corresponding to the first localization or cracking condition in concrete under consideration of arbitrary thermo-mechanical conditions were developed in the framework of the Modified TD-LDP model for porous materials like concrete. Then, numerical evaluations of the localization conditions and cracking directions were performed for a wide spectrum of stress and temperature conditions and considering drained and undrained hydraulic conditions. The results in this work demonstrate that temperature is a key aspect regarding failure mode and critical cracking directions of concrete. This is valid for all stress paths in the compression regime. The numerical and analytical results with the Modified TD-LDP model demonstrate that the stability condition at peak under plane strain state is much more affected by temperature than that corresponding to plane stress. Although at room temperature, plane strain conditions potential the overall stability and the diffusion of concrete failure as compared to the plane stress case, this situation is less pronounced under increasing temperature. This is a relevant conclusion in this paper regarding temperature effects on concrete failure modes.

Brittle or localized failure modes are also exhibited in the uniaxial tensile test (for all possible temperatures), and in the pure shear test under plane stress conditions. Finally, and as said before, localized failure in plane strain states takes place only under high temperature.

All together, the numerical and analytical solutions for discontinuous bifurcation of temperature-dependent gradient poroplastic media in this work offer great potentials for more accurate predictions and understanding of concrete failure modes under different thermomechanical scenarios, and of their sensitivity to temperature.

Acknowledgements The authors acknowledge the financial support for this work by CONICET (National Council for Science and Technology) through the Grant PIP No. 112-2011010-1079 and by CIUNT (Research Council of the University of Tucuman, Argentina) through the Grant No. 26/E-511.

Table 2 Critical localization directions for uniaxial tension/compression, biaxial compression and pure shear tests at variable temperature

Temperature (°C)	Critical localization angles (°)—plane stress state/plane strain state			
	Uniaxial compression	Biaxial compression	Pure shear	Uniaxial tension
20	36.56–143.44	63.56–116.44	21.93–158.07	0–180
	32.46–147.54	50.16–123.84	14.82–165.18	0–180
250	37.68–142.32	65.81–114.19	23.65–156.35	0–180
	34.14–145.86	53.34–126.66	19.32–160.68	0–180
500	38.25–141.75	66.94–113.06	24.75–155.25	0–180
	35.64–144.36	57.60–122.40	22.14–157.80	0–180

Localized failure cases are underlined

Appendix A: Temperature-dependent flow theory for non-local poroplasticity

The rates of the plastic strains, plastic fluid mass and hardening/softening variables are

$$\dot{\boldsymbol{\varepsilon}}^p = \dot{\lambda}\,\Phi^*{}_{,\boldsymbol{\sigma}}, \quad \dot{m}^p = \dot{\lambda}\,\Phi^*{}_{,p}, \quad \dot{q}_\alpha = \dot{\lambda}\,\Phi^*{}_{,Q_\alpha}, \tag{37}$$

being $\dot{\lambda}$ the plastic parameter rate, $\Phi^* = \Phi^*(\boldsymbol{\sigma}, p, \theta, Q_\alpha)$ and $\Phi = \Phi(\boldsymbol{\sigma}, p, \theta, Q_\alpha)$ the plastic potential and yield condition, respectively. Note that symbology $\Phi^*{}_{,b}$ indicates partial derivatives of Φ^* respect to b. Total dissipative stresses are computed as the addition of local and non-local contributions $Q_\alpha = Q_\alpha^l + Q_\alpha^g$, while the consistency condition results

$$\dot{\Phi} = \Phi_{,\boldsymbol{\sigma}} : \dot{\boldsymbol{\sigma}} + \Phi_{,p}\,\dot{p} + \Phi_{,\theta}\,\dot{\theta} + \Phi_{,Q_\alpha}\,\dot{Q}_\alpha = 0\,. \tag{38}$$

Therefore, the following differential equation for the plastic multiplier can be obtained for the undrained case under homogeneous conditions ($\nabla Q_\alpha = \mathbf{0}$) and non-local dissipative stresses independent of temperature gradients

$$\dot{\lambda} h + \dot{\Phi}^{trial} + \dot{\Phi}^g = 0. \tag{39}$$

The generalized local plastic modulus and the rates of the local and gradient loading functions are computed as

$$\begin{aligned} h = &-\Phi_{,\boldsymbol{\sigma}} : \boldsymbol{E} : \Phi^*{}_{,\boldsymbol{\sigma}} \\ &+\frac{M}{\rho_f}\,\Phi_{,\boldsymbol{\sigma}} : \boldsymbol{B}\,\Phi^*{}_{,p} - \frac{M}{\rho_f}\Phi_{,p}\,\Phi^*{}_{,p} \\ &+M\Phi_{,p}\,\boldsymbol{B} : \Phi^*{}_{,\boldsymbol{\sigma}} - H_\alpha^l \Phi_{,Q_\alpha}\,\Phi^*{}_{,Q_\alpha}\,, \\ \dot{\Phi}^{trial} = &-\Phi_{,\boldsymbol{\sigma}}\,\boldsymbol{E} : \dot{\boldsymbol{\varepsilon}} \end{aligned} \tag{40}$$

$$\begin{aligned} &-\frac{M}{\rho_f}\,\Phi_{,\boldsymbol{\sigma}} : \boldsymbol{B}\,\dot{m} + \Phi_{,\boldsymbol{\sigma}} : \boldsymbol{A}\dot{\theta} + \frac{M}{\rho_f}\Phi_{,p}\,\dot{m} \\ &-\Phi_{,p}\,M\boldsymbol{B} : \dot{\boldsymbol{\varepsilon}} + \Phi_{,p}\,\rho_f\,\chi\dot{\theta} \\ &+\left(s_{fr}^{(q_\alpha)}{}_{,q_\alpha} + \Phi_{,\theta}\right)\dot{\theta}, \end{aligned} \tag{41}$$

$$\begin{aligned} \dot{\Phi}^g = &-\frac{l_c^2}{2\theta} H_\alpha^g\,\Phi_{,Q_\alpha}\nabla q_\alpha \cdot \nabla\dot{\theta} + \frac{l_c^2}{2\theta} H_\alpha^g\,\Phi_{,Q_\alpha}\,\nabla\theta \cdot \nabla q_\alpha\dot{\theta} \\ &+2l_c^2 H_\alpha^g\,\Phi_{,Q_\alpha}\,\Phi^*{}_{,Q_\alpha}\,\nabla q_\alpha \cdot \nabla\dot{\lambda} \\ &-\frac{l_c^2}{2\theta} H_\alpha^g\,\Phi_{,Q_\alpha}\,\Phi^*{}_{,Q_\alpha}\,\nabla\theta \cdot \nabla\dot{\lambda}\,, \end{aligned} \tag{42}$$

respectively, being H_α^l the local-plastic hardening/softening modulus, H_α^g the gradient softening modulus and l_c the gradient characteristic length. Under similar assumptions and for the drained case, Eq. (39) can be rewritten as

$$h_d\dot{\lambda} + \dot{\Phi}_d^{trial} + \dot{\Phi}_d^g = 0\,, \tag{43}$$

being

$$h_d = -\Phi_{,\boldsymbol{\sigma}} \cdot \boldsymbol{E}^s \cdot \Phi^*{}_{,\boldsymbol{\sigma}} - \Phi_{,Q_\alpha}\,H_\alpha^l \Phi^*{}_{,Q_\alpha}\,, \tag{44}$$

$$\begin{aligned} \dot{\Phi}_d^{trial} = &\,\Phi_{,\boldsymbol{\sigma}} : \boldsymbol{E}^s : \dot{\boldsymbol{\varepsilon}} + \left(\Phi_{,p} - \Phi_{,\boldsymbol{\sigma}} : \boldsymbol{B}\right)\dot{p} \\ &+\left(-\Phi_{,\boldsymbol{\sigma}} : \boldsymbol{A} + \Phi_{,Q_\alpha}\,H^\theta + \Phi_{,\theta}\right)\dot{\theta}, \end{aligned} \tag{45}$$

$$\dot{\Phi}_d^g = l_c^2 H_\alpha^g\,\Phi_{,Q_\alpha}\,\Phi^*{}_{,Q_\alpha}\,\nabla^2\dot{\lambda}. \tag{46}$$

By replacing $\dot{\lambda}$ from Eqs. (39) and (43) in Eqs. (5) and (8), the constitutive relations for both undrained and drained conditions result

$$\begin{aligned} \dot{\boldsymbol{\sigma}} = &\,\boldsymbol{E} : \dot{\boldsymbol{\varepsilon}} - \frac{M}{\rho_f}\,\dot{m}\,\boldsymbol{B} + \left(\frac{M}{\rho_f}\,\Phi^*{}_{,p} - \boldsymbol{E} : \Phi^*{}_{,\boldsymbol{\sigma}}\right) \\ &\left[-\frac{\left(\dot{\Phi}^{trial} + \dot{\Phi}^g\right)}{h}\right] - \boldsymbol{A}\,\dot{\theta}, \end{aligned} \tag{47}$$

$$\dot{\boldsymbol{\sigma}} = \boldsymbol{E}^s : \dot{\boldsymbol{\varepsilon}} - \boldsymbol{E}^s : \Phi^*{}_{,\boldsymbol{\sigma}} \left[-\frac{\left(\dot{\Phi}_d^{trial} + \dot{\Phi}_d^g\right)}{h_d}\right]$$

$$-\boldsymbol{B}\,\dot{p} - \boldsymbol{A}^{s}\,\dot{\theta}. \tag{48}$$

Finally, Eqs. (47) and (48) can be rewritten as

$$\dot{\boldsymbol{\sigma}} = \boldsymbol{E}^{ep} : \dot{\boldsymbol{\varepsilon}} + {}^{m}\boldsymbol{E}^{ep}\,\dot{m} + \boldsymbol{E}^{g}\,\dot{\Phi}^{g} + {}^{\theta}\boldsymbol{E}^{ep}\,\dot{\theta}, \tag{49}$$

$$\dot{\boldsymbol{\sigma}} = {}^{s}\boldsymbol{E}^{ep} : \dot{\boldsymbol{\varepsilon}} + {}^{md}\boldsymbol{E}^{ep}\,\dot{p} + {}^{d}\boldsymbol{E}^{g}\,\dot{\Phi}^{g}_{d} + {}^{\theta d}\boldsymbol{E}^{ep}\,\dot{\theta}, \tag{50}$$

respectively, with the elastoplastic tensors

$$\begin{aligned}\boldsymbol{E}^{ep} = \boldsymbol{E} - \frac{1}{h+h^{g}}\big[&\boldsymbol{E} : \Phi^{*}{}_{,\boldsymbol{\sigma}} \otimes \Phi_{,\boldsymbol{\sigma}} : \boldsymbol{E} \\ &- \left(\frac{M}{\rho_f}\right)^{2} \Phi_{,p}\,\Phi^{*}{}_{,p}\,\boldsymbol{B}\otimes\boldsymbol{B} \\ &+ \frac{M}{\rho_f}(\Phi_{,p}\boldsymbol{E} : \Phi^{*}{}_{,\boldsymbol{\sigma}} \otimes \boldsymbol{B} \\ &+ \Phi^{*}{}_{,p}\,\boldsymbol{B}\otimes\Phi_{,\boldsymbol{\sigma}} : \boldsymbol{E})\big],\end{aligned} \tag{51}$$

$$\begin{aligned}{}^{m}\boldsymbol{E}^{ep} = -\frac{M}{\rho_f}\Bigg[&\boldsymbol{B} - \frac{1}{h}\left(\frac{M}{\rho_f}\Phi^{*}{}_{,p}\,\Phi_{,p}\,\boldsymbol{B}\right. \\ &- \frac{M}{\rho_f}\,\Phi^{*}{}_{,p}\,\Phi_{,\boldsymbol{\sigma}}\,\boldsymbol{B} : \boldsymbol{B} - \boldsymbol{E} : \Phi^{*}{}_{,\boldsymbol{\sigma}}\,\Phi_{,p} \\ &\left.+ \boldsymbol{E} : \Phi^{*}{}_{,\boldsymbol{\sigma}}\,\Phi_{,\boldsymbol{\sigma}} : \boldsymbol{B}\right)\Bigg],\end{aligned} \tag{52}$$

$$\begin{aligned}{}^{\theta}\boldsymbol{E}^{ep} = \frac{1}{h}\Bigg(&\boldsymbol{E} : \Phi^{*}{}_{,\boldsymbol{\sigma}} \otimes \Phi_{,\boldsymbol{\sigma}} : \boldsymbol{A} - \chi\boldsymbol{E} : \Phi^{*}{}_{,\boldsymbol{\sigma}}\,\Phi_{,p} \\ &- \frac{M}{\rho_f}\Phi^{*}{}_{,p}\,\boldsymbol{B}\,\Phi_{,\boldsymbol{\sigma}} : \boldsymbol{A} + \chi\frac{M}{\rho_f}\Phi^{*}{}_{,p}\,\Phi_{,p}\,\boldsymbol{B}\Bigg),\end{aligned} \tag{53}$$

$${}^{s}\boldsymbol{E}^{ep} = \boldsymbol{E}^{s} - \frac{1}{h_d}\left(\Phi_{,\boldsymbol{\sigma}} : \boldsymbol{E}^{s} \otimes \boldsymbol{E}^{s} : \Phi^{*}{}_{,\boldsymbol{\sigma}}\right), \tag{54}$$

$${}^{md}\boldsymbol{E}^{ep} = -\frac{1}{h_d}\left(\Phi_{,p} - \Phi_{,\boldsymbol{\sigma}} : \boldsymbol{B}\right)\boldsymbol{E}^{s} : \Phi^{*}{}_{,\boldsymbol{\sigma}} - \boldsymbol{B}, \tag{55}$$

$${}^{d}\boldsymbol{E}^{g} = -\frac{1}{h_d}\boldsymbol{E}^{s} : \Phi^{*}{}_{,\boldsymbol{\sigma}}, \tag{56}$$

$${}^{\theta d}\boldsymbol{E}^{ep} = -\frac{1}{h_d}\Phi_{,\boldsymbol{\sigma}} : \boldsymbol{A}^{s} \otimes \boldsymbol{E}^{s} : \Phi^{*}{}_{,\boldsymbol{\sigma}} + \boldsymbol{A}^{s}. \tag{57}$$

Appendix B: Critical bifurcation directions and hardening modulus

Taking into account that

$$\overline{\Phi}_{,\boldsymbol{\sigma}} = \Phi_{,\boldsymbol{\sigma}} - \frac{1}{3}\left(\Phi_{,\boldsymbol{\sigma}}\right)_{V}\boldsymbol{I}, \quad \overline{\Phi^{*}}_{,\boldsymbol{\sigma}} = \Phi^{*}{}_{,\boldsymbol{\sigma}} - \frac{1}{3}\left(\Phi^{*}{}_{,\boldsymbol{\sigma}}\right)_{V}\boldsymbol{I}, \tag{58}$$

where $\overline{\Phi}_{,\boldsymbol{\sigma}}$ and $\overline{\Phi^{*}}_{,\boldsymbol{\sigma}}$ are the deviatoric components of $\Phi_{,\boldsymbol{\sigma}}$ and $\Phi^{*}{}_{,\boldsymbol{\sigma}}$, respectively, while considering a volumetric non-associated flow rule, i.e.

$$\left(\Phi_{,\boldsymbol{\sigma}}\right)_{V} \neq \left(\Phi^{*}{}_{,\boldsymbol{\sigma}}\right)_{V} \quad \text{and} \quad \overline{\Phi^{*}}_{,\boldsymbol{\sigma}} = \overline{\Phi}_{,\boldsymbol{\sigma}} \tag{59}$$

then, it can be concluded that solutions of Eq. (36) depend on the sign of the following coefficients (according Mroginski and Etse 2014)

$$c_{13} = \overline{\Phi}_{,\sigma_1} + (1-2\alpha_0)\,\overline{\Phi}_{,\sigma_3} + r\,, \tag{60}$$

$$c_{31} = \overline{\Phi}_{,\sigma_3} + (1-2\alpha_0)\,\overline{\Phi}_{,\sigma_1} + r\,, \tag{61}$$

being

$$r = \alpha_2\left[\left(\Phi_{,\boldsymbol{\sigma}}\right)_{V} + \left(\Phi^{*}{}_{,\boldsymbol{\sigma}}\right)_{V}\right] - \alpha_3\left(\Phi_{,p} + \Phi^{*}{}_{,p}\right), \tag{62}$$

$$k = -\frac{1}{2}\left(\overline{\Phi}_{,\sigma_i}\right)^{2} + \alpha_1\left(\Phi_{,\boldsymbol{\sigma}}\right)_{V}\left(\Phi^{*}{}_{,\boldsymbol{\sigma}}\right)_{V} + \alpha_5\Phi_{,p}\,\Phi^{*}{}_{,p}\,, \tag{63}$$

with

$$\alpha_0 = \phi, \tag{64}$$

$$\alpha_1 = \frac{\lambda_L^{'}(1-\phi)}{G}\left(\frac{1}{3} + \frac{\lambda_L^{'}}{4G}\right) - \left(\frac{\lambda_L^{'}}{4G} + \frac{\phi}{9} + \frac{1}{18}\right), \tag{65}$$

$$\alpha_2 = \frac{1-\phi}{3} + \frac{\lambda_L^{'}(1-\phi)}{2G}, \quad \alpha_3 = \frac{Mb\,(1-\phi)}{2G}, \tag{66}$$

$$\alpha_4 = \frac{Mb}{4G}\left[1 - (1-\phi)\,\frac{\lambda_L^{'}}{G}\right] - \frac{Mb\,(1-\phi)}{6G}, \tag{67}$$

$$\alpha_5 = (1-\phi)\left(\frac{Mb}{2G}\right)^{2} - \frac{M}{4G}. \tag{68}$$

Finally, the solutions of $\overline{H}^{l}_{crit}$ and its critical directions $\boldsymbol{n}$, are obtained for different cases

(a) $r \geq 0$ and $c_{31} \geq 0$

$$\begin{aligned}\overline{H}^{l}_{crit} &= 4G\,(1-\alpha_0)\left(\overline{\Phi}_{,\sigma_1}\right)^{2} + r\,\overline{\Phi}_{,\sigma_1} \\ &\quad + \alpha_4\left[\Phi_{,p}\left(\Phi^{*}{}_{,\boldsymbol{\sigma}}\right)_{V} + \Phi^{*}{}_{,p}\left(\Phi_{,\boldsymbol{\sigma}}\right)_{V}\right] + k - \frac{h^{g}}{4G} \\ &\overline{\Phi}_{,\sigma_1} > \overline{\Phi}_{,\sigma_2} > \overline{\Phi}_{,\sigma_3} \Rightarrow \boldsymbol{n}_1^{2} = 1, \quad \boldsymbol{n}_2^{2} = 0, \quad \boldsymbol{n}_3^{2} = 0 \\ &\overline{\Phi}_{,\sigma_1} = \overline{\Phi}_{,\sigma_2} > \overline{\Phi}_{,\sigma_3} \Rightarrow \boldsymbol{n}_1^{2} + \boldsymbol{n}_2^{2} = 1, \quad \boldsymbol{n}_3^{2} = 0 \\ &\overline{\Phi}_{,\sigma_1} > \overline{\Phi}_{,\sigma_2} = \overline{\Phi}_{,\sigma_3} \Rightarrow \boldsymbol{n}_1^{2} = 1, \quad \boldsymbol{n}_2^{2} = \boldsymbol{n}_3^{2} = 0\end{aligned} \tag{69}$$

(b) $r \geq 0$ and $c_{13} \leq 0$ or $r \leq 0$ and $c_{13} \geq 0$

$$\begin{aligned}\overline{H}^{l}_{crit} = &\frac{G}{\alpha_0}\left(\overline{\Phi}_{,\sigma_1} + \overline{\Phi}_{,\sigma_3} + r\right)^{2} - \overline{\Phi}_{,\sigma_1}\overline{\Phi}_{,\sigma_3} \\ &+ \alpha_4\left[\Phi_{,p}\left(\Phi^{*}{}_{,\boldsymbol{\sigma}}\right)_{V} + \Phi^{,*}_{p}\left(\Phi_{,\boldsymbol{\sigma}}\right)_{V}\right] \\ &+ k - \frac{h^{g}}{4G}\end{aligned} \tag{70}$$

$$\overline{\Phi}_{,\sigma_1} > \overline{\Phi}_{,\sigma_2} > \overline{\Phi}_{,\sigma_3} \Rightarrow n_1^2 = \frac{c_{13}}{2\alpha_0\left(\overline{\Phi}_{,\sigma_1} - \overline{\Phi}_{,\sigma_3}\right)},$$
$$n_2^2 = 0, \quad n_3^2 = -\frac{c_{31}}{2\alpha_0\left(\overline{\Phi}_{,\sigma_1} - \overline{\Phi}_{,\sigma_3}\right)} \tag{71}$$
$$\overline{\Phi}_{,\sigma_1} = \overline{\Phi}_{,\sigma_2} > \overline{\Phi}_{,\sigma_3} \Rightarrow \boldsymbol{n}_1^2 + \boldsymbol{n}_2^2 = \frac{c_{13}}{2\alpha_0\left(\overline{\Phi}_{,\sigma_1} - \overline{\Phi}_{,\sigma_3}\right)},$$
$$\boldsymbol{n}_3^2 = -\frac{c_{31}}{2\alpha_0\left(\overline{\Phi}_{,\sigma_1} - \overline{\Phi}_{,\sigma_3}\right)} \tag{72}$$
$$\overline{\Phi}_{,\sigma_1} > \overline{\Phi}_{,\sigma_2} = \overline{\Phi}_{,\sigma_3} \Rightarrow \boldsymbol{n}_1^2 = \frac{c_{13}}{2\alpha_0\left(\overline{\Phi}_{,\sigma_1} - \overline{\Phi}_{,\sigma_3}\right)},$$
$$\boldsymbol{n}_2^2 + \boldsymbol{n}_3^2 = -\frac{c_{31}}{2\alpha_0\left(\overline{\Phi}_{,\sigma_1} - \overline{\Phi}_{,\sigma_3}\right)} \tag{73}$$

(c) $r \leq 0$ and $c_{13} \leq 0$

$$\overline{H}^l_{crit} = 4G\,(1-\alpha_0)\left(\overline{\Phi}_{,\sigma_3}\right)^2 + r\,\overline{\Phi}_{,\sigma_3} + \alpha_4\left[\Phi_{,p}\left(\Phi^*_{,\boldsymbol{\sigma}}\right)_V + \left(\Phi_{,\boldsymbol{\sigma}}\right)_V\right] + k - \frac{h^g}{4G} \tag{74}$$
$$\overline{\Phi}_{,\sigma_1} > \overline{\Phi}_{,\sigma_2} > \overline{\Phi}_{,\sigma_3} \Rightarrow \boldsymbol{n}_1^2 = 0, \quad \boldsymbol{n}_2^2 = 0, \quad \boldsymbol{n}_3^2 = 1$$
$$\overline{\Phi}_{,\sigma_1} = \overline{\Phi}_{,\sigma_2} > \overline{\Phi}_{,\sigma_3} \Rightarrow \boldsymbol{n}_1^2 = \boldsymbol{n}_2^2 = 0, \quad \boldsymbol{n}_3^2 = 1$$
$$\overline{\Phi}_{,\sigma_1} > \overline{\Phi}_{,\sigma_2} = \overline{\Phi}_{,\sigma_3} \Rightarrow \boldsymbol{n}_1^2 = 0, \quad \boldsymbol{n}_2^2 + \boldsymbol{n}_3^2 = 1$$

Some derivatives in Eqs. (69)–(74) have been already particularized for the TD-LDP model in Eqs. (31) and (32), while the other ones are

$$\overline{\Phi}_{,\boldsymbol{\sigma}} = \overline{\Phi}^*_{,\boldsymbol{\sigma}} = \left[3\,\alpha(\theta) + \frac{\beta(\theta)\,n_0}{\sqrt{6}\,{}^*\tau}\right]\frac{1}{f_c'^2}\boldsymbol{S} \tag{75}$$

$$\left(\Phi_{,\boldsymbol{\sigma}}\right)_V = \frac{\beta(\theta)\,n_0}{f_c'} \tag{76}$$

$$\left(\Phi^*_{,\boldsymbol{\sigma}}\right)_V = \frac{\beta(\theta)\,\eta\,n_0}{f_c'}. \tag{77}$$

References

Abellan MA, de Borst R (2006) Wave propagation and localisation in a softening two-phase medium. Comput Methods Appl Mech 195:5011–5019

Benallal A, Comi C (2002) Material instabilities in inelastic saturated porous media under dynamic loadings. Int J Solids Struct 39(13–14):3693–3716

Borja RI (2004) Cam-clay plasticity. Part V: A mathematical framework for threephase deformation and strain localization analyses of partially saturated porous media. Comput Methods Appl Mech 193:5301–5338

Coussy O (1995) Mechanics of porous continua. Wiley, Hoboken

Di Maio A., Hirschi F., Giaccio G., Zerbino R (1999) Hormigones expuestos a altas temperaturas: evaluacin de la permeabilidad y otras propiedades fisicas. Anales SAM, 204–209

Ehlers W, Graf T, Ammann M (2004) Deformation and localization analysis of partially saturated soil. Comput Methods Appl Mech 193(27–29):2885–2910

Ekh M, Grymer M, Runesson K, Svedberg T (2007) Gradient crystal plasticity as part of the computational modelling of polycrystals. Int J Numer Methods Eng 72(2):197–220

Gawin D, Pesavento F, Schrefler BA (2004) Modelling of deformations of high strength concrete at elevated temperatures. Mater Struct 37:218–236

Geers MG, Kouznetsova V, Brekelmans W (2010) Multi-scale computational homogenization: trends and challenges. J Comput Appl Math 234(7):2175–2182

Gernay T, Millard A, Franssen JM (2013) A multiaxial constitutive model for concrete in the fire situation: theoretical formulation. Int J Solids Struct 50:3659–3673

Hadamard J (1903) Propagation des ondes et les equations d'Hydrodynamique. Chelsea, New York

Hager I (2013) Behaviour of cement concrete at high temperature. Bull Pol Acad Sci Tech Sci 61(1):1–10

Hammoud R, Yahia A, Boukhili R (2014) Triaxial compressive strength of concrete subjected to high temperatures. J Mater Civ Eng 26:705–712

Henann DL, Kamrin K (2014) Continuum thermomechanics of the nonlocal granular rheology. Int J Plast 60:145–162

Janotka I, Bagel L (2002) Pore structures, permeabilities, and compressive strengths of concrete at temperatures up to 800 °C. ACI Mater J 100:196–200

Jirásek M, Rolshoven S (2009) Localization properties of strain-softening gradient plasticity models. Part I. Int J Solids Struct 46:2225–2238

Jirásek M, Rolshoven S (2009) Localization properties of strain-softening gradient plasticity models. Part II. Int J Solids Struct 46:2239–2254

Kalifa P, Menneteau FD, Quenard D (2000) Spalling and pore pressure in HPC at high temperatures. Cem Concr Res 30:1915–1927

Kang H, Willam K (1999) Localization characteristics of a triaxial concrete model. ASCE-JEM 125:941–950

Kristensson O, Ahadi A (2005) Numerical study of localization in soil systems. Comput Geotech 32(8):600–612

Lee J, Xi Y, Willam K (2008) Properties of concrete after high-temperature heating and cooling. ACI Mater J 105:334–341

Liu X, Scarpas A, Blaauwendraad J (2005) Numerical modelling of nonlinear response of soil. Part 2: strain localization investigation on sand. Int J Solids Struct 42(7):1883–1907

Mihashi H, Numao T, Fukuzawa K (1992) Simultaneous heat and mass transfer in heated concrete. In: 3rd international workshop: behaviour of concrete elements under thermal and hygral gradients. Weimar, Germany

Mindeguia JC, Pimienta P, Noumowé A, Kanema M (2010) Temperature, pore pressure and mass variation of concrete subjected to high temperature: experimental and numerical discussion on spalling risk. Cem Concr Res 40:477–487

Mroginski JL, Etse G (2014) Discontinuous bifurcation analysis of thermodynamically consistent gradient poroplastic materials. Int J Solids Struct 51:1834–1846

Oliver J, Caicedo M, Roubin E, Huespe A, Hernandez J (2015) Continuum approach to computational multiscale modeling of propagating fracture. Comput Methods Appl Mech Eng 294:384–427

Ortiz M (1987) An analytical study of the localized failure modes of concrete. Mech Mater 62:159–174

Ottosen NS, Runesson K (1991) Properties of discontinuous bifurcation solutions in elasto-plasticity. Int J Solids Struct 27:401–421

Ottosen NS, Runesson K, Peric D (1991) Discontinuous bifurcations of elastic-plastic solids at plane stress and plane strain. Int J Plast 7:99–121

Pereira F, Pistol K, Korzen M, Weise F, Pimienta P, Carré H, Huismann S (2011) Monitoring of fire damage processes in concrete by pore pressure and acoustic emission measurements. In: Proceedings of 2nd international RILEM workshop on concrete spalling due to fire exposure, 5–7 October, Delft, The Netherlands, pp 69–77

Ripani M, Etse G, Vrech S, Mroginski J (2014) Thermodynamic gradient-based poro-plastic theory for concrete under high temperatures. Int J Plast 61:157–177

Rudnicki J, Rice J (1975) Conditions for the localization of deformation in pressure-sensitive dilatant materials. J Mech Phys Solids 23:371–394

Runesson K, Perić D, Sture S (1996) Effect of pore fluid compressibility on localization in elastic-plastic porous solids under undrained conditions. Int J Solids Struct 33(10):1501–1518

Sabatini PJ, Finno RJ (1996) Effect of consolidation on strain localization of soft clays. Comput Geotech 18(4):311–339

Schiava R, Etse G (2006) Constitutive modelling and discontinuous bifurcation assessment in unsaturated soils. J Appl Mech 73(6):1039–1044

Sulem J (2010) Bifurcation theory and localization phenomena. Eur J Environ Civ Eng 14(1–10):989–1009

Svedberg T, Runesson K (1997) A thermodynamically consistent theory of gradient-regularized plasticity coupled to damage. Int J Plast 13(6–7):669–696

Tenchev R, Purnell P (2005) An application of a damage constitutive model to concrete at high temperature and prediction of spalling. Int J Solids Struct 42:6550–6565

Toro S, Snchez PJ, Blanco PJ, de Souza Neto EA, Huespe AE, Feijo RA (2016) Multiscale formulation for material failure accounting for cohesive cracks at the macro and micro scales. Int J Plast 76:75–110

Tsagrakis I, Konstantinidis A, Aifantis E (2003) Strain gradient and wavelet interpretation of size effects in yield and strength. Mech Mater 35:733–745

Vrech S, Etse G (2006) Geometrical localization analysis of gradient-dependent parabolic Drucker–Prager elastoplasticity. Int J Plast 22:943–964

Vrech S, Etse G (2007) FE approach for thermodynamically consistent gradient-dependent Plasticity. Lat Am Appl Res 37:127–132

Vrech S, Etse G (2009) Gradient and fracture energy-based plasticity theory for quasi-brittle materials like concrete. Comput Methods Appl Mech 199(1–4):136–147

Vrech S, Etse G (2012) Discontinuous bifurcation analysis in fracture energy-based gradient plasticity for concrete. Int J Solids Struct 49:1294–1303

Xargay H, Folino P, Sambataro L, Etse G (2018) Temperature effects on failure behavior of self-compacting high strength plain and fiber reinforced concrete. Constr Build Mater 165:723–734

Xotta G, Beizaee S, Willam KJ (2016) Bifurcation investigations of coupled damage-plasticity models for concrete materials. Comput Methods Appl Mech 298(1):428–452

Zhang HL, Davie CT (2013) A numerical investigation of the influence of pore pressures and thermally induced stresses for spalling of concrete exposed to elevated temperatures. Fire Saf J 59:102–110

Zhang HW, Schrefler BA (2001) Uniqueness and localization analysis of elastic–plastic saturated porous media. Int J Numer Anal Methods 25(1):29–48

Zhang YQ, Hao H, Yu M-H (2002) Effect of porosity on the properties of strain localization in porous media under undrained conditions. Int J Solids Struct 39(7):1817–1831

Zhen W, Sun D, Chen Y (2010) Analytical solution and numerical simulation of shear bands along different stress paths in three-dimensional stress state. Soil Behav Geo-Micromech 200:192–197